



CHICAGO JOURNALS



Reconstruction of High Dynamic Range Images: Simulations of LBT Observations of a Stellar Jet, a Pathfinder Study for Future AO-Assisted Giant Telescopes

Author(s): A. La Camera, S. Antonucci, M. Bertero, P. Boccacci, D. Lorenzetti, B. Nisini and C. Arcidiacono

Source: *Publications of the Astronomical Society of the Pacific*, (-Not available-), p. 000

Published by: [The University of Chicago Press](#) on behalf of the [Astronomical Society of the Pacific](#)

Stable URL: <http://www.jstor.org/stable/10.1086/675509>

Accessed: 05/02/2014 10:05

Your use of the JSTOR archive indicates your acceptance of the Terms & Conditions of Use, available at <http://www.jstor.org/page/info/about/policies/terms.jsp>

JSTOR is a not-for-profit service that helps scholars, researchers, and students discover, use, and build upon a wide range of content in a trusted digital archive. We use information technology and tools to increase productivity and facilitate new forms of scholarship. For more information about JSTOR, please contact support@jstor.org.



The University of Chicago Press and Astronomical Society of the Pacific are collaborating with JSTOR to digitize, preserve and extend access to *Publications of the Astronomical Society of the Pacific*.

<http://www.jstor.org>

Reconstruction of High Dynamic Range Images: Simulations of LBT Observations of a Stellar Jet, a Pathfinder Study for Future AO-Assisted Giant Telescopes

A. LA CAMERA,¹ S. ANTONIUCCI,² M. BERTERO,¹ P. BOCCACCI,¹ D. LORENZETTI,² B. NISINI,² AND C. ARCIDIACONO³

Received 2013 December 05; accepted 2014 January 09; published 2014 February 4

ABSTRACT. We present simulated Large Binocular Telescope (LBT) infrared narrow-band observations of a star-jet system, in conjunction with improved and optimized deconvolution and image reconstruction algorithms, considering two cases of interest: single-dish direct imaging with an AO-assisted camera and imaging through a Fizeau interferometer that combines the beams of the two mirrors of LBT. We aim at understanding what accuracy can be obtained with the use of present AO-assisted large telescopes (such as LBT) and what improvements an interferometric instrument (such as LINC-NIRVANA) will be able to provide. The proposed deconvolution method is based on the target decomposition as a sum of a point source (the star) and an extended source (the jet). By assuming Poisson noise we add to the negative logarithm of the likelihood a regularization term enforcing smoothness of the jet component. Finally, we use a Richardson-Lucy-like method for the minimization of this function. This approach is an improvement of a method proposed by Lucy in 1994 for accurate photometric restoration of HST images and called two channel photometric restoration. We denote the new method as the multi-component Richardson-Lucy (MC-RL) method. The analysis of the reconstructed objects shows that the MC-RL method applied to the interferometric observations allows us to evaluate the width and the spatial intensity profile of the jet down to 20 mas with an accuracy better than about 20% in the best case of a central star fainter than 10 mag. These limits allow us to obtain a very good reconstruction of the jet acceleration region very close to the exciting source, which would provide fundamental scientific information on the jet collimation degree and eventually on its launching mechanism. As concerns the proposed MC-RL method, it demonstrates a good performance in the reconstruction of images with a very high dynamic range. It can be improved in several directions, by increasing both its efficiency, thanks to recently proposed acceleration techniques, and its accuracy by means of more sophisticated regularization terms. We are also planning to apply the method to simulated observations of upcoming super giant earth-based telescopes.

Online material: color figures

1. INTRODUCTION

The recent advances in adaptive optics (AO) and infrared detectors technologies are the key ingredients of the development of high resolution imaging from ground-based telescopes. The quality of AO-corrected images can be further improved through post-AO reprocessing algorithms: the original science frame can be reconstructed by applying appropriate point-spread function (PSF) deconvolution methods. The deconvolution and reconstruction process can be particularly challenging for high contrast images, i.e., when one is interested in detecting

a faint signal close to a very bright star. This is the case, for instance, for detections of orbiting exo-planets and brown dwarfs, or observations of circumstellar structures around Young Stellar Objects (YSOs).

A specific case that strongly benefits from the combination of high angular resolution and high contrast imaging is the study of jets in YSOs. Jets originate in the inner circumstellar disks of YSOs (i.e., within ~ 1 AU from the star). Only optical-infrared interferometers like VLTI and CHARA can access this inner region, but at very limited sensitivity. However, magneto-hydrodynamical models for the jet launching mechanism predict that most of the jets' collimation and acceleration occur in a region of the jet < 50 AU, corresponding to $\lesssim 0.3''$ for objects in the nearest star-forming clouds at a distance of ~ 150 pc (e.g., Konigl & Pudritz 2000), i.e., a region that is now accessible with IR AO-corrected instrumentation. In this context, it is of paramount importance to understand how well we can overcome the difficulty in imaging a faint jet close to a bright YSO due to the contrast with the source itself.

¹DIBRIS, Università di Genova, Via Dodecaneso 35, 16146, Genova, Italy, andrea.lacamera@unige.it, bertero@disi.unige.it, patrizia.boccacci@unige.it.

²INAF—Osservatorio Astronomico di Roma, Via di Frascati 33, 00040, Monteporzio Catone, Italy, simone.antonucci@oa-roma.inaf.it, dario.lorenzetti@oa-roma.inaf.it, brunella.nisini@oa-roma.inaf.it.

³INAF—Osservatorio Astronomico di Bologna, Via Ranzani 1, 40127 Bologna, Italy, carmelo.arcidiacono@oabo.inaf.it.

To this aim, we are exploring the feasibility of investigating the inner regions of jets in YSOs through imaging with narrow band filters centered on typical infrared emission lines. In particular, we present here simulated Large Binocular Telescope (LBT) (Hill 2010) observations of a star-jet system, in conjunction with the relative deconvolution and image reconstruction algorithms. We consider two cases of interest: direct imaging with an AO-assisted camera and imaging through a Fizeau interferometer that combines the beams of the two 8.4 m mirrors of LBT (like the forthcoming LINC-NIRVANA [LN] instrument). The comparison between these two cases will allow us to understand what precision can be obtained with the present LBT instrumentation and what improvements an instrument such as LN will be able to provide.

We recall that LN⁴ (Herbst et al. 2003) is one of the two Fizeau interferometers of the Large Binocular Telescope (LBT). They can operate as true imagers because the two beams from the primary mirrors are combined in a common focal plane. The point spread function (PSF) of LN will be that of a 8.4 m mirror (the diameter of the two mirrors of LBT) modulated by the interference fringes. Since the distance between the centers of the two mirrors is 14.4 m, the maximum baseline of LN will be of 22.8 m. It follows that the resolution of a single LN image is not uniform because it is that of a 22.8 m telescope in the direction of the baseline and that of a 8.4 m telescope in the orthogonal direction. In order to get a uniform resolution, and precisely that of a 22.8 m telescope, it will be necessary to acquire different images of the same scientific object corresponding to different orientations of the baseline and to combine these images into a unique one by means of suitable image reconstruction methods.

In previous studies (Ciliegi et al. 2008), we have already considered the reconstruction of LN-images of a YSO model simulated by means of the software package AIRY-LN (Desiderà et al. 2008). The used reconstruction algorithm was an iterative multiple-image deconvolution method derived from the Richardson-Lucy (RL) (Richardson 1972; Lucy 1974) algorithm. However, we obtained unsatisfactory reconstruction of the jet region close to the emitting star, because standard deconvolution methods are unable to provide sufficiently accurate reconstructions of a scientific object formed by a bright star superimposed onto a weaker, diffuse component such as the emitted jet.

A way for circumventing this difficulty is to model the scientific object as the sum of two components: a point source (the star) and an extended source (the jet); moreover, different regularization terms for the two components should be introduced in the objective function to be minimized. Recently several methods have been introduced for this approach and a short review is provided by Giovannelli & Coulais (2005), who also

propose a method suitable for radio interferometry. A common feature of these methods is that they are based on a least-square formulation, hence on the assumption of additive Gaussian noise.

A similar approach, but in the framework of Poisson noise, was proposed by L. B. Lucy (Lucy 1994; Hook & Lucy 1994) and called by the authors *two-channel photometric restoration*. This was re-proposed in La Camera et al. (2012), but with a different regularization term and a different iteration scheme. This method, which we called *multi-component Richardson-Lucy* (MC-RL), is further investigated and applied in this paper both for single-image and multiple-image deconvolution (Bertero et al. 2011), the latter being the problem arising for any Fizeau interferometer. In order to study the feasibility of the method we will explore different star-jet intensity contrast cases by varying the magnitude of the star at each simulation. This test will ultimately define the limits of applicability of the reconstruction procedure to real cases.

On the basis of the results obtained here for the LBT telescope and as a follow-up project, we plan to apply the MC-RL method to the case of observations with future 30 m-class telescopes, like the Giant Magellan Telescope (GMT), the Thirty Meter Telescope (TMT) or the European Extremely Large Telescope (E-ELT).

The paper is organized as follows: in sec. 2 we describe the proposed deconvolution method both for single dish telescope and LN interferometer; in sec. 3 we outline the generation of the simulated LBT observations for the two cases and we give details on the deconvolution of the simulated images; finally, in sec. 4 we describe the analysis performed on the reconstructed images in order to quantify the validity of the method and to define the limits of its application in the case of the stellar jet observations. Conclusions are summarized in sec. 5.

2. IMAGE DECONVOLUTION

In this section we describe the proposed deconvolution method. We first introduce its general features and, successively, we provide the two versions for single dish telescope and LN interferometer, respectively.

2.1. The MC-RL Method

A common problem in different kinds of astrophysical imaging is to reconstruct two maps of a given region: one consisting uniquely of stars (point sources, PS) and the other representing the smooth structures underlying the stars (extended sources, ES). Several recent papers have been devoted to image deconvolution with point and smooth source separation (De Mol & Defrise 2004; Giovannelli & Coulais 2005; Ayasso et al. 2012). A common feature of these approaches is to consider a least-square framework (hence additive Gaussian noise) with the introduction of different regularization terms for the point and smooth components, as well as constraints

⁴ Please see <http://www.mpia.de/LINC/>.

such as the nonnegativity of the solution. However, as is well-known, in astronomical imaging the noise is a mixture of Poisson noise, due to the counting process, and additive Gaussian noise, due to the read-out noise (RON) (Snyder et al. 1994). As shown in Snyder et al. (1995) a simplified model can be obtained by treating the RON as a Poisson process in a suitable way and we use this approach in this paper.

To our knowledge, the first approach based on the separation of a PS and ES component in the framework of Poisson noise is due to L. B. Lucy (1994), with the additional assumption that the PS component consists of a number of designed stars with known locations. Since these can be taken as point sources, modeled by delta functions, the PS component is zero everywhere except at the known locations of the point sources. Therefore, we can write the unknown scientific object $f(\mathbf{n})$ as $f(\mathbf{n}) = f_P(\mathbf{n}) + f_E(\mathbf{n})$, where:

1. $\mathbf{n} = \{n_1, n_2\}$ is a multi-index labeling the pixels of the image;

2. f_P is the point-source (PS) component given by

$$f_P(\mathbf{n}) = \sum_{j=1}^q c_j \delta(\mathbf{n}, \mathbf{n}_j), \quad (1)$$

where the \mathbf{n}_j are the known positions of the q stars in the image array and the c_j are the unknown emission intensities;

3. f_E is the unknown extended-source (ES) component.

For the specific problem we are considering, the point source is a single star, so that $f_P(\mathbf{n}) = c_0 \delta(\mathbf{n}, \mathbf{n}_0)$. This structure of f_P , used in the reconstruction algorithm, is a very strong constraint and is automatically satisfied by the proposed iterative algorithm if it is satisfied by the initial guess. Therefore we do not need the introduction of regularization terms as concerns the PS component. On the other hand, a regularization will be introduced for the ES component. We do not use the entropy term as in Lucy (1994) and Hook & Lucy (1994) because, as is known, this term can enforce sparsity (Donoho et al. 1992). Therefore, as in La Camera et al. (2012), we use a regularization term enforcing smoothness such as the ℓ_2 norm of the ES component. Our algorithm can be easily extended to other kinds of regularization, if given in terms of differentiable functions.

2.1.1. Single-Image Deconvolution

As already shown using the approximation of the RON proposed by Snyder et al. (1995), we can assume that the image is uniquely corrupted by Poisson noise. In such a case, as shown for instance in Bertero et al. (2009), by neglecting constant factors the negative logarithm of the likelihood is given by the generalized Kullback-Leibler (KL) divergence, also known as Csiszár I-divergence (Csiszár 1991). Therefore, the maximum likelihood (ML) solutions are the pairs $\{f_P, f_E\}$ which minimize the following function

$$J_0(f_P, f_E; g) = \sum_{\mathbf{n} \in S} \{g(\mathbf{n}) \ln \frac{g(\mathbf{n})}{[H(f_P + f_E)](\mathbf{n}) + b(\mathbf{n})} + [H(f_P + f_E)](\mathbf{n}) + b(\mathbf{n}) - g(\mathbf{n})\}, \quad (2)$$

where:

1. g is the sum of the detected image and of the variance σ^2 of the RON, according to the approach proposed by Snyder et al. (1995) for RON compensation;

2. accordingly, b is the sum of the (estimated) background emission and of σ^2 ;

3. H is the imaging matrix, given in terms of the (known) space-invariant point spread function (PSF) K

$$(Hf)(\mathbf{n}) = (K * f)(\mathbf{n}), \quad \sum_{\mathbf{n} \in S} K(\mathbf{n}) = 1, \quad (3)$$

where $K * f$ denotes convolution.

The function J_0 is nonnegative, convex and coercive as a function of $f = f_P + f_E$ and therefore has the same properties as a function of the two blocks of variables f_P and f_E , as well as of the pair $\mathbf{f} = \{f_P, f_E\}$. As is well-known, the absolute minimizers of J_0 appear as *sky-night solutions* (Barrett & Meyers 2003), i.e., as a set of bright spots over a black background, and therefore they could be satisfactory for the PS component but not for the ES one. For this reason, we add a smoothing regularization term to the KL divergence, depending only on f_E . This approach can be justified in the framework of a Bayesian formulation of the problem (Bertero et al. 2009), if the *prior* is given by a suitable Gibbs distribution.

We consider the most simple regularization term of the Tikhonov type, namely the ℓ_2 norm of the ES component. In conclusion, we propose to minimize the following objective function

$$J_\mu(f_P, f_E; g) = J_0(f_P, f_E; g) + \frac{\mu}{2} \sum_{\mathbf{n} \in S} |f_E(\mathbf{n})|^2, \quad (4)$$

where μ is a regularization parameter to be estimated. We discuss this point in the next section.

For the minimization of this function with respect to the pair $\mathbf{f} = \{f_P, f_E\}$, we use a scaled gradient method as suggested by the split-gradient method (SGM) introduced in Lantéri et al. (2002). To this purpose, we denote $\nabla J_\mu(\mathbf{f}; g)$ the gradient of J_μ with respect to \mathbf{f} , which is given by the pair of gradients $\nabla_P J_\mu, \nabla_E J_\mu$ with respect to the variables f_P, f_E , respectively. Using the well known expression of the gradient of $J_0(f; g)$, in the case of a normalized PSF, we obtain

$$\begin{aligned} \nabla_P J_\mu(f_P, f_E; g) &= \hat{1} - H^T \frac{g}{Hf + b}, \\ \nabla_E J_\mu(f_P, f_E; g) &= \hat{1} - H^T \frac{g}{Hf + b} + \mu f_E, \end{aligned} \quad (5)$$

where $f = f_P + f_E$ as above and $\hat{1}$ is the array with all elements equal to 1. Here and in the following the product and the quotient of two arrays are defined in the Hadamard sense, i.e., pixel by pixel. Then the algorithm is as follows

$$\mathbf{f}^{(k+1)} = \mathbf{f}^{(k)} - \lambda_k \mathbf{S}^{(k)} \cdot \nabla J_\mu(\mathbf{f}^{(k)}; g), \quad (6)$$

where \cdot denotes pixel by pixel multiplication, $\mathbf{S}^{(k)}$ is the pair of scaling arrays

$$S_P^{(k)} = f_P^{(k)}, \quad S_E^{(k)} = \frac{f_E^{(k)}}{\hat{1} + \mu f_E^{(k)}}, \quad (7)$$

and λ_k is a suitable parameter obtained by a line search along the descent direction, using for instance Armijo rule (Lantéri et al. 2002), which assures convergence of the algorithm. Numerical experience demonstrates that this is true even if we set $\lambda_k = 1$, a choice which allows us to reduce the computational burden of the algorithm. In such a case it takes the very simple form:

1. Give nonnegative $f_P^{(0)}, f_E^{(0)}$.
2. For $k = 0, 1, \dots$ compute

$$\begin{aligned} f_P^{(k+1)} &= f_P^{(k)} H^T \frac{g}{H f^{(k)} + b} \\ f_E^{(k+1)} &= \frac{f_E^{(k)}}{\hat{1} + \mu f_E^{(k)}} H^T \frac{g}{H f^{(k)} + b} \\ f^{(k+1)} &= f_P^{(k+1)} + f_E^{(k+1)}. \end{aligned} \quad (8)$$

3. Stop the iteration according to a given stopping rule.

A few comments on this algorithm that, as mentioned in the Introduction, we denote as the MC-RL method. Each step consists of an RL iteration on f_P and of an SGM iteration on f_E ; therefore, the result of each iteration is automatically nonnegative. Moreover, as already remarked, an important point is the initialization. If we choose $f_P^{(0)}(\mathbf{n}) = \delta(\mathbf{n}, \mathbf{n}_0)$, then one can easily check that, at iteration k , we have $f_P^{(k)}(\mathbf{n}) = c^{(k)} \delta(\mathbf{n}, \mathbf{n}_0)$, where $c^{(k)}$ is the reconstructed star intensity, converging to the flux of the star. If we remark that $(H f^{(k)}) (\mathbf{n}) = c^{(k)} K(\mathbf{n} - \mathbf{n}_0) + (H f_E^{(k)}) (\mathbf{n})$, then the first step of the iteration can also be written in the simpler form

$$c^{(k+1)} = c^{(k)} \left[H^T \frac{g}{c^{(k)} K_0 + H f_E^{(k)} + b} \right] (\mathbf{n}_0), \quad (9)$$

where $K_0(\mathbf{n}) = K(\mathbf{n} - \mathbf{n}_0)$. As concerns $f_E^{(0)}$ we initialize with a constant array; since we do not have information on the flux of the jet we simply take $f_E^{(0)} = \hat{1}$ and also in this case we have verified in our simulations that the algorithm is able to reproduce the correct flux value.

In the case where several stars are present in the field-of-view, then it is sufficient to initialize the iteration by taking $f_P^{(0)}$ as in equation (1), with an initial guess for the c_j , their values being improved by the subsequent iterations. Again, one can easily check that each $f_P^{(k)}$ has the same structure.

Convergence of the previous algorithm is not proved; however, in our numerical experiments we always find convergent sequences of iterations. The algorithm is slow, since it requires thousands of iterations. However, since it is a scaled gradient method, one can obtain a convergent and faster algorithm in the framework of the recently proposed *Scaled Gradient Projection* (SGP) method (Bonettini et al. 2009). In the case of f_P , one can use the projection on the convex set of the linear combination of delta-arrays corresponding to the PS component.

2.1.2. Multiple-Image Deconvolution

As briefly recalled in the introduction, a single image of the LN interferometer, as that of any Fizeau interferometer, is characterized by an anisotropic resolution, so that for obtaining a reconstructed image with the best resolution in all the directions (that of the 22.8 m baseline in the case of LN) one must acquire different images of the same target with different orientations of the baseline and combine these images in a unique one by means of an appropriate deconvolution algorithm. In general a small number of suitable orientations (from 3 to 5) is sufficient for obtaining a good coverage in Fourier space (Bertero & Boccacci 2000).

If p different images g_1, \dots, g_p are available (for simplicity, we will denote by \mathbf{g} the set of these images), since they are statistically independent, then equation (2) is replaced by the following one (Bertero et al. 2011)

$$\begin{aligned} J_0(f_P, f_E; \mathbf{g}) &= \sum_{j=1}^p \sum_{\mathbf{n} \in S} \{g_j(\mathbf{n}) \ln \frac{g_j(\mathbf{n})}{[H_j(f_P + f_E)](\mathbf{n}) + b_j(\mathbf{n})} \\ &\quad + [H_j(f_P + f_E)](\mathbf{n}) + b_j(\mathbf{n}) - g_j(\mathbf{n})\}, \end{aligned} \quad (10)$$

where $H_j f = K_j * f$, K_j being the PSF associated with the image g_j .

If $J_\mu(f_P, f_E; \mathbf{g})$ is defined as in equation (4), then it is easy to verify that its gradients, defined as in equation (6), are given by

$$\begin{aligned} \nabla_P J_\mu(f_P, f_E; \mathbf{g}) &= p \hat{1} - \sum_{j=1}^p H_j^T \frac{g_j}{H_j f + b_j}, \\ \nabla_E J_\mu(f_P, f_E; \mathbf{g}) &= p \hat{1} - \sum_{j=1}^p H_j^T \frac{g_j}{H_j f + b_j} + \mu f_E. \end{aligned} \quad (11)$$

Therefore the algorithm of equation (8) is replaced by the following one.

1. Give nonnegative $f_P^{(0)}, f_E^{(0)}$.
2. For $k = 0, 1, \dots$ compute

$$\begin{aligned}
 f_P^{(k+1)} &= \frac{1}{p} f_P^{(k)} \sum_{j=1}^p H_j^T \frac{g_j}{H_j f^{(k)} + b_j} \\
 f_E^{(k+1)} &= \frac{f_E^{(k)}}{p\hat{1} + \mu f_E^{(k)}} \sum_{j=1}^p H_j^T \frac{g_j}{H_j f^{(k)} + b_j} \\
 f^{(k+1)} &= f_P^{(k+1)} + f_E^{(k+1)}.
 \end{aligned} \tag{12}$$

3. Stop the iteration according to a given stopping rule.

Our remarks on the algorithm of equation (8) apply also to this one.

2.1.3. Boundary Effect Correction

In our simulations, as a consequence of the brightness of the star and of the extent of the PSF, a part of the star image lies beyond the boundary of the considered field-of-view (FoV): see, for instance, the last panel of Figure 1. In order to obtain accurate results we decided to use in our code a method for the correction of boundary effects. This method is based on an approach proposed in Bertero & Boccacci (2005) for single image deconvolution and in Anconelli et al. (2006) for multiple image deconvolution. The basic idea is to merge the detected image into a broader array by zero padding and to reconstruct the unknown object on this array. If at the end of the deconvolution

procedure one takes the restriction of the object to the domain corresponding to that of the detected image, the result is practically free of annoying boundary artifacts. A downloadable algorithm applicable both to single and multiple image deconvolution is described and tested in Prato et al. (2012).

2.2. Choice of the Regularization Parameter

The proposed algorithms provide the solution of the regularized deconvolution problems. Indeed, in the case of the PS component, regularization is provided by the knowledge of the star location while, in the case of the ES component, regularization is provided by the addition of a penalty quadratic term. Therefore, in principle, iterations must be pushed to convergence. The result is not sensible if the choice of the regularization parameter is not correct.

The problem of the choice of μ in the case of regularization of the generalized KL divergence is basically an open problem and, to our knowledge, only a few criteria have been proposed until now (Bardsley & Golde 2009; Bertero et al. 2010). In this paper, since the number of detected photons in an astronomical image is quite large, we adopt the criterion proposed in Bertero et al. (2010) because it is asymptotic in this limit. It is based on the following result

$$\lim_{N^2} \frac{2}{N^2} J_0(\tilde{f}; g) = 1, \tag{13}$$

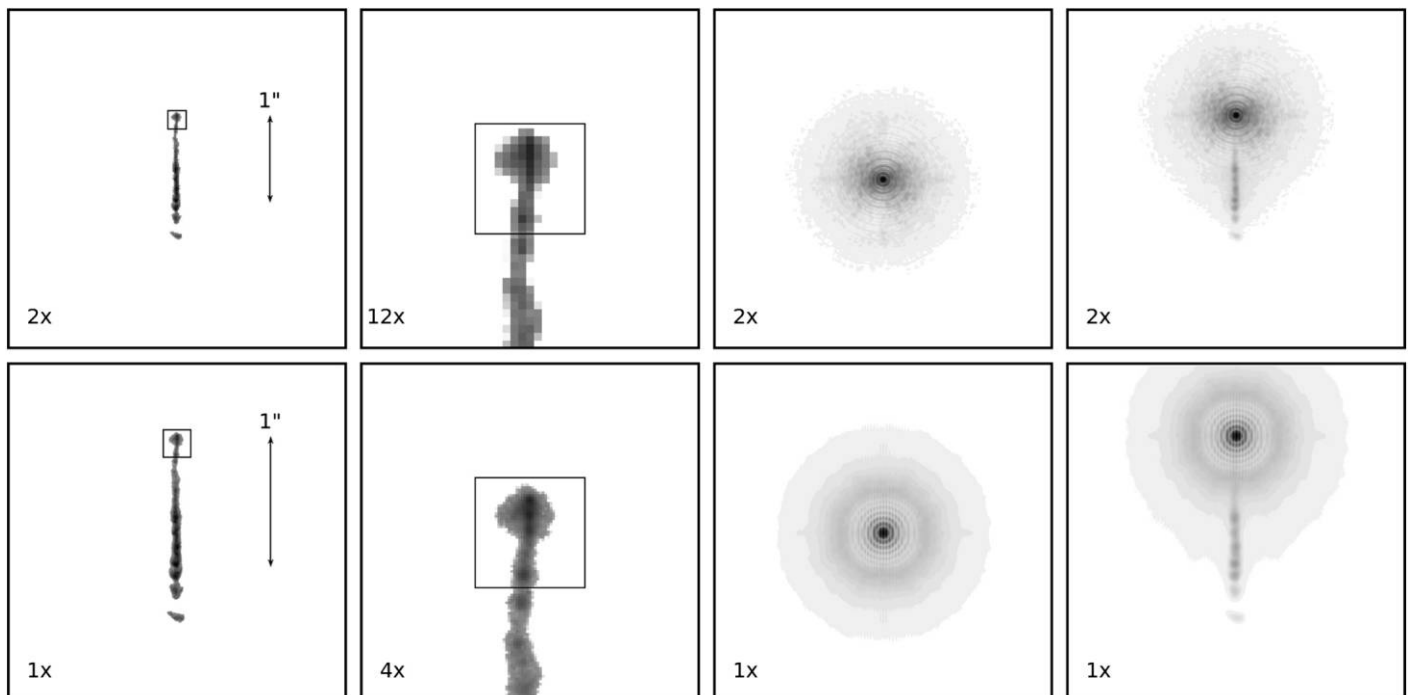


FIG. 1.—(Top panels, from left to right): Case 1 object and a detailed view of the region around the star (*not shown*) with the square box described in the text; the PSF used for convolution and the image in the case of $m_s = 8$. (Bottom panels, from left to right:) the same for Case 2, for the angle corresponding to 0° . All images are shown in log-scale.

where N^2 is the number of pixels, \tilde{f} is the ground-truth, i.e., the astronomical target generating the image g , and the limit is for observation time tending to infinity, i.e., number of counts tending to infinity. However, the relationship is already satisfied for reasonable observation times.

Another result proved in Bertero et al. (2010) is that, if we denote the minimizer of the function (4) as f_μ , then the function defined by

$$D_g(\mu) = \frac{2}{N^2} J_0(f_\mu; g) \quad (14)$$

is an increasing function of μ . As verified in our simulations this function starts from a value smaller than 1 for $\mu = 0$ and crosses 1 for a certain value of μ . Therefore, we can select this value as an ‘‘optimal’’ one since it provides a reconstructed object f_μ which gives the value of $D_g(\mu)$ corresponding to the ground-truth. The monotonic behaviour of $D_g(\mu)$ assures that, if this value exists, then it is unique. The function $D_g(\mu)$ is called the *discrepancy function* and the selection criterion based on this function is called the *discrepancy principle*. It is obvious that this criterion can be used also in the case of multiple images (LN).

The criterion can be applied to the deconvolution of observed images. Therefore it is convenient to verify its validity by means of numerical experiments where the ground-truth is known. To this purpose, for a given μ , one can compute the relative root-mean-square (RMS) error given by

$$\rho(\mu) = \frac{\|f_\mu - \tilde{f}\|}{\|\tilde{f}\|}, \quad (15)$$

where $\|\cdot\|$ denotes the ℓ_2 norm, and search for the value of μ minimizing this quantity. However, in the case of a very bright star, i.e., the case investigated in this paper, f_μ is dominated by the star contribution so that this criterion may not be very significant. To this purpose it is convenient to compute the error on the ES component and therefore we consider the quantity

$$\rho_E(\mu) = \frac{\|f_{E,\mu} - \tilde{f}_E\|}{\|\tilde{f}_E\|}, \quad (16)$$

where $f_{E,\mu}$ and \tilde{f}_E are the ES components of f_μ and \tilde{f} , respectively. We call this quantity the *restoration error* and we compare the value of μ obtained by its minimization with that provided by the discrepancy principle.

3. SIMULATION OF LBT OBSERVATIONS

3.1. Synthetic Objects

We simulated the observations of a near-IR jet in a narrow band filter centered on the [FeII] 1.64 μm line. This is motivated by the fact that stellar jets are line emission objects

and [FeII] transitions are the brightest atomic lines observable in the near-IR (e.g., Nisini et al. 2002). We obtained the ground-truth (the object) for our simulations from an optical image taken with HST of the HH34 jet (Reipurth et al. 2002). Starting from this image, two different objects have been generated for our tests. In the first case (Case 1), the original image has been downsampled by a factor 3 and immersed into a 256×256 array, surrounded by zeros. A pixel scale of 15 mas/pixel has been assumed as typical scale of a camera attached to a single LBT dish.

In the second case (Case 2), the original object (not resampled) has been inserted into a 512×512 array with the LN pixel scale of 5 mas/pixel. In both cases, we assumed an integrated magnitude of the object of 14.5 mag in a [FeII] filter ($\lambda = 1.64 \mu\text{m}$, $\Delta\lambda = 0.025 \mu\text{m}$) within a square region surrounding the position where the HH34 infrared driving source is located. This corresponds to a typical brightness of the [FeII] 1.64 μm line of about $5 \times 10^{-14} \text{ W m}^{-2} \mu\text{m}^{-1} \text{ arcsec}^{-2}$ (Agra-Amboage et al. 2011). The two objects, as well as a zoom around the selected square region, are shown in the left and middle-left panels of Figure 1. Finally, to each of these two images, in the pixel corresponding to the source, a point star with variable magnitude (from 8 to 11 mag in the same [FeII] filter) was added in order to simulate cases at different contrasts, for a total of four different objects for each case.

3.2. Simulated Images

For each object of Case 1 (corresponding to stars with $m_s = 8, \dots, 11$ and representing the single LBT dish), a 256×256 image has been obtained by convolving the object with an AO-corrected PSF with Strehl ratio (SR) equal to 0.67, already used in Desiderà & Carillet (2009) and produced by means of the Software Package CAOS (Carillet et al. 2004).

Concerning Case 2, relative to the LN case, for each object four equispaced 512×512 images, at $0^\circ, 45^\circ, 90^\circ$, and 135° , have been obtained by convolving the object with four PSFs with a SR ~ 0.7 . The PSFs have been generated by the software LOST (Arcidiacono et al. 2004).

To all convoluted images we added, as background emission, an average H-band sky brightness of 13.5 mag/arcsec² and we corrupted the results with Poisson and additive Gaussian noise ($\sigma = 10 e^-/\text{pixel}$). For each case (single image in Case 1 and each hour angle image in Case 2) we assumed an integration time of 30 minutes. The two PSFs used for convolution and the two images corresponding to the case of $m_s = 8$ are shown, respectively, in middle-right and right panels of Figure 1.

3.3. Deconvolution of the Simulated Images

The deconvolution of the simulated images has been performed with the MC-RL method by utilizing the same PSFs used for their generation. In this way one should obtain the best target reconstruction possible starting from the input data.

The main astrophysical interest in the reconstructed object is centered on the region of the extended component close to the star. For this reason, together with the restoration error $\rho_E(\mu)$ defined in equation (16), we define $\rho'_E(\mu)$ as a similar function, computed considering only the pixels of $f_{E,\mu}$ and \tilde{f}_E within the

region surrounding the star (14×14 pixels for Case 1 and 42×42 pixels for Case 2, shown in Fig. 1).

In our simulations, at each iteration and for a given value of the regularization parameter μ , we computed the KL divergence as defined in equation (4) and we stopped the algorithms

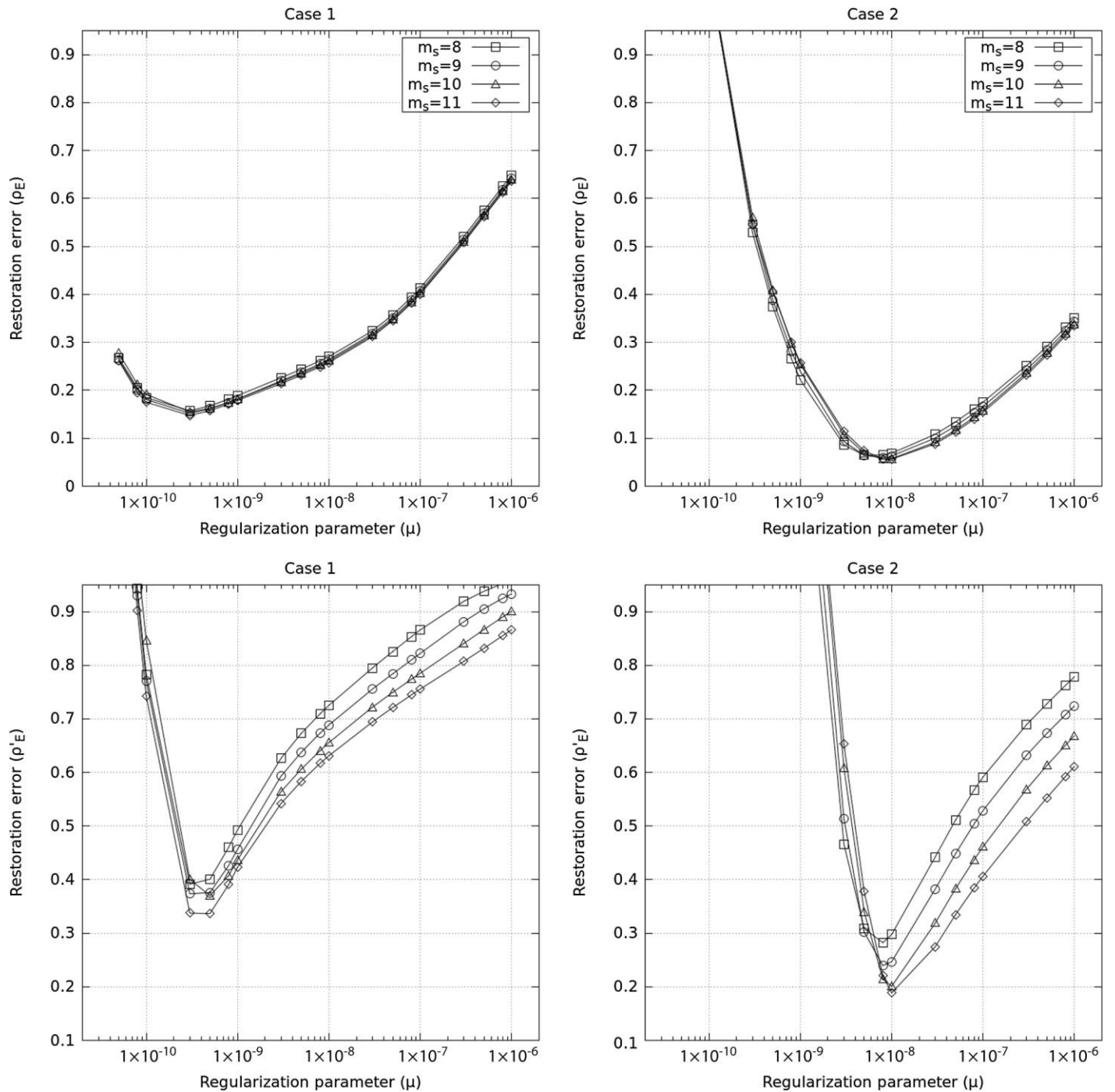


FIG. 2.—Restoration error as a function of the regularization parameter (μ) for Case 1 (left panels) and Case 2 (right panels). The restoration error ρ_E computed on the full image is shown in the top panels, while ρ'_E computed on the small square box surrounding the star is shown in the bottom panels.

TABLE 1

VALUES OF μ CORRESPONDING TO MINIMUM RESTORATION ERRORS OF THE JET FOR THE TWO CASES AND FOR THE FOUR MAGNITUDES OF THE STAR, I.E., THE MINIMUM POINTS OF THE CURVES IN FIG. 2.

THE PAIRS (μ, ρ_E) ARE GIVEN IN THE SECOND AND THIRD COLUMN, WHILE THE PAIRS (μ', ρ'_E) ARE GIVEN IN THE LAST TWO COLUMNS.

m_s	μ	ρ_E	μ'	ρ'_E
Case 1				
8	3.0×10^{-10}	15.74%	3.0×10^{-10}	39.13%
9	3.0×10^{-10}	15.19%	3.0×10^{-10}	37.35%
10	3.0×10^{-10}	15.50%	5.0×10^{-10}	37.01%
11	3.0×10^{-10}	14.74%	5.0×10^{-10}	33.68%
Case 2				
8	8.0×10^{-9}	6.47%	8.0×10^{-9}	28.24%
9	8.0×10^{-9}	5.99%	8.0×10^{-9}	23.96%
10	8.0×10^{-9}	5.62%	1.0×10^{-8}	20.01%
11	1.0×10^{-8}	5.62%	1.0×10^{-8}	18.87%

(eqs. [8] and [13]) when this function became constant. More precisely, according to a given tolerance tol (for example $\text{tol} = 10^{-6}$), we stopped the iterations when

$$\left| J_\mu \left(f_P^{(k)}, f_E^{(k)}; g \right) - J_\mu \left(f_P^{(k-1)}, f_E^{(k-1)}; g \right) \right| \leq \text{tol} \cdot J_\mu \left(f_P^{(k)}, f_E^{(k)}; g \right). \quad (17)$$

At the end of the iterations, we have final values of the restoration errors $\rho_E(\mu)$ and $\rho'_E(\mu)$ and we show these values as

functions of μ in Figure 2. For each case and for each magnitude of the star, the error curves show a minimum that suggests an optimal value of the regularization parameter, even if the value that minimizes ρ_E could not be the same of that one that minimizes ρ'_E . In fact, in Case 1 the value of μ that gives the minimum restoration error ρ_E is the same for all magnitudes, while in Case 2 only the last value for $m_s = 11$ is slightly different from the other ones. Concerning the partial restoration error ρ'_E , we have a similar behaviour, even if the values in these cases are not always the same. The pairs (μ, ρ_E) and (μ', ρ'_E) representing the minimum points of each curve are collected in Table 1.

We recall that the *discrepancy principle* (Bertero et al. 2010) can be used in order to choose the regularization parameter, especially if we are using real observed images. Again, we pushed the algorithm to convergence and, at the end of the iterations, we computed the value of the discrepancy function $D_g(\mu)$. In our tests concerning Case 1, the value of μ at which $D_g(\mu)$ crosses 1 is larger than the value that minimizes the two restoration errors. Indeed, as shown in Figure 3, the four curves cross the value 1 for $\mu \sim 3 \times 10^{-9}$, an order of magnitude greater than the optimal value. On the other end, in Case 2, the principle gives a value very close to the optimal one, i.e., $\mu \sim 1 \times 10^{-8}$.

4. DATA ANALYSIS

To test the goodness and limits of the presented method for deriving useful scientific information, we have analysed the reconstructions by considering both the total profile flux at a given position along the jet, i.e., the flux integrated in the direction

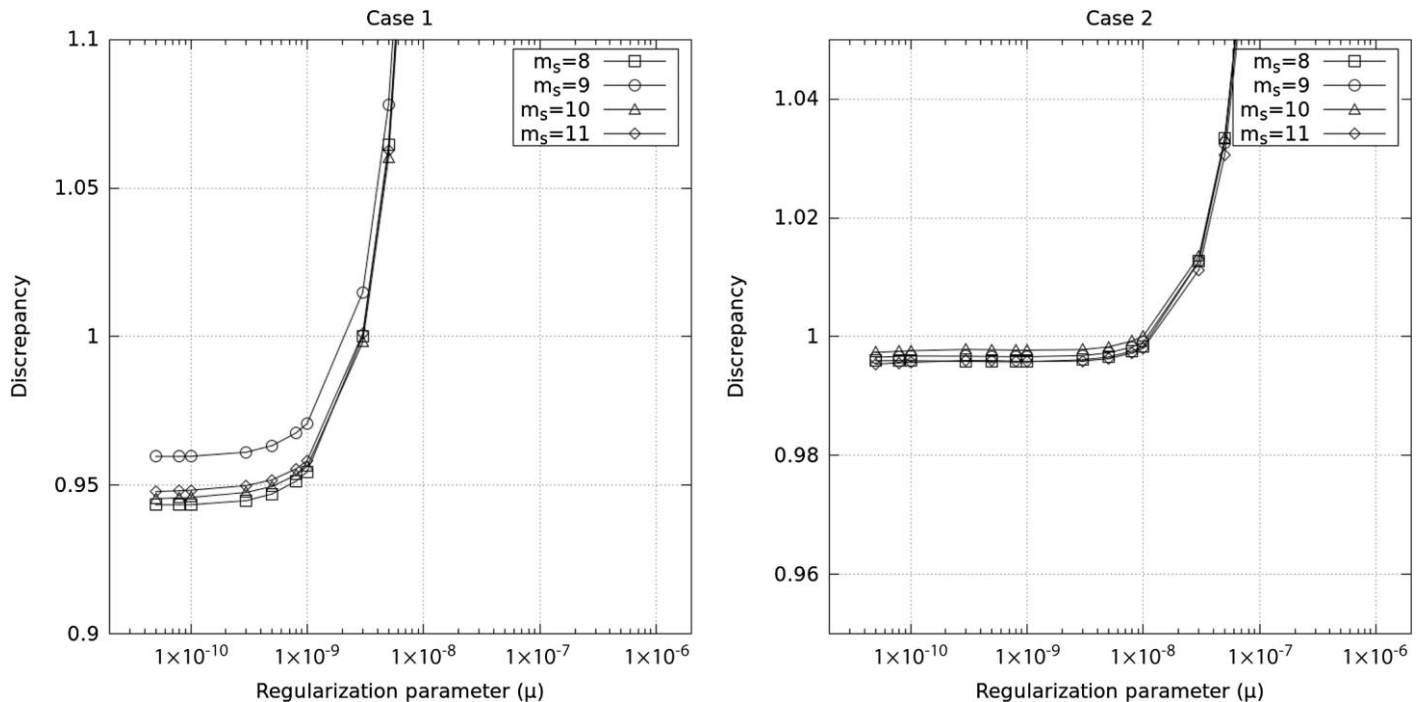


FIG. 3.—Discrepancy D_g as a function of the regularization parameter (μ) for Case 1 (left panel) and Case 2 (right panel).

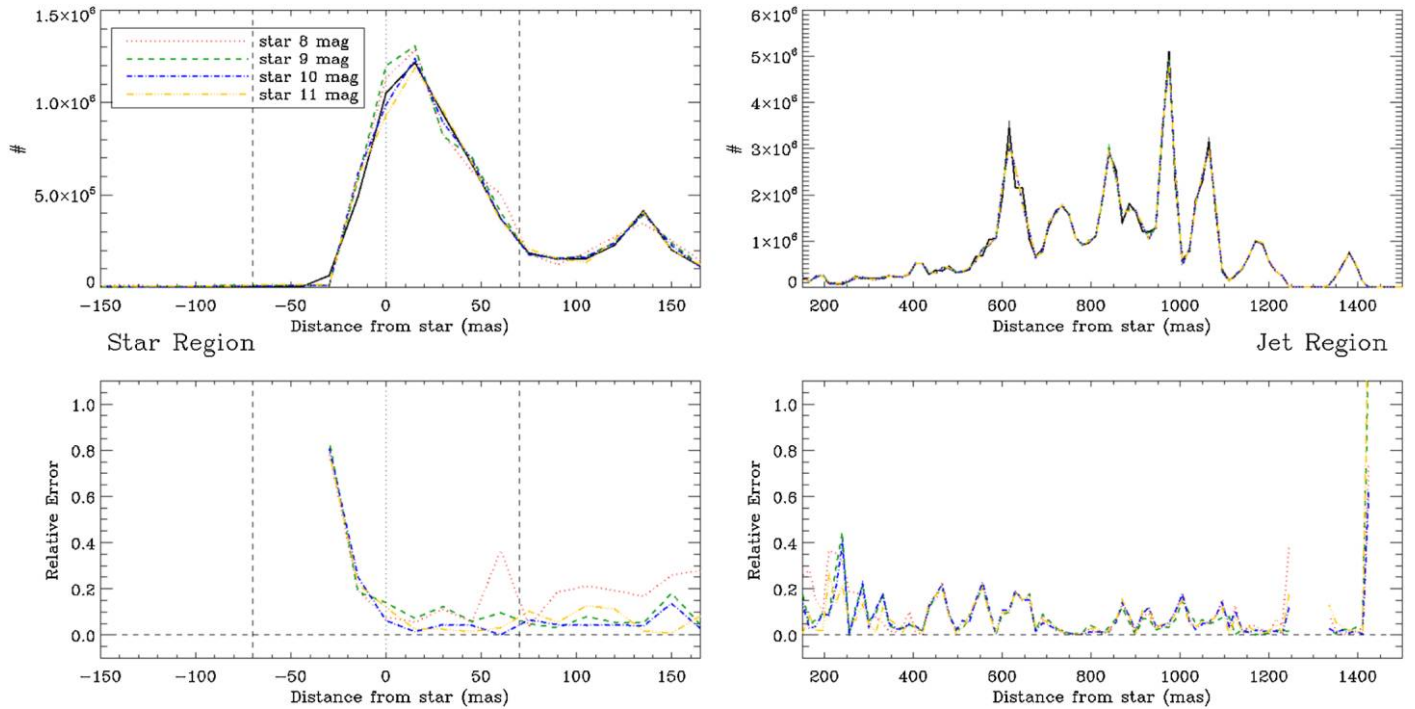


FIG. 4.—Case 1 observations: integrated flux along the spatial profile of the jet (orthogonal to its axis) as a function of the distance from the star. The reconstructions for the different central star magnitudes (lines of different colors and styles, see legend) are compared to the reference object (thick black line). We show in separate panels the region close to the star (left) and the remainder of the jet (right). The vertical dashed lines mark the region within 70 mas from the star, corresponding to a physical size of about 10 AU for a star at a distance of 150 pc. The bottom panels show the relative error of the reconstructed images. See the electronic edition of the *PASP* for a color version of this figure.

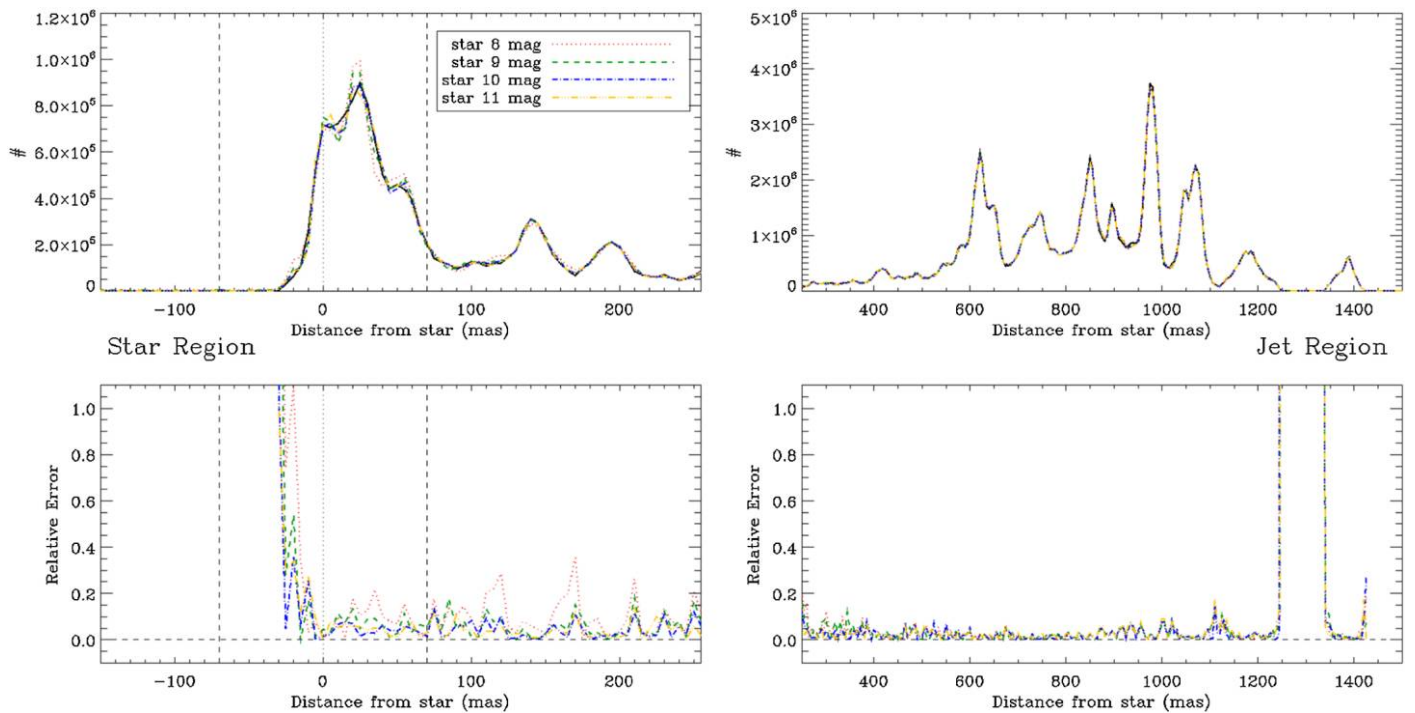


FIG. 5.—Same as Fig. 4 for Case 2 (interferometric observations). See the electronic edition of the *PASP* for a color version of this figure.

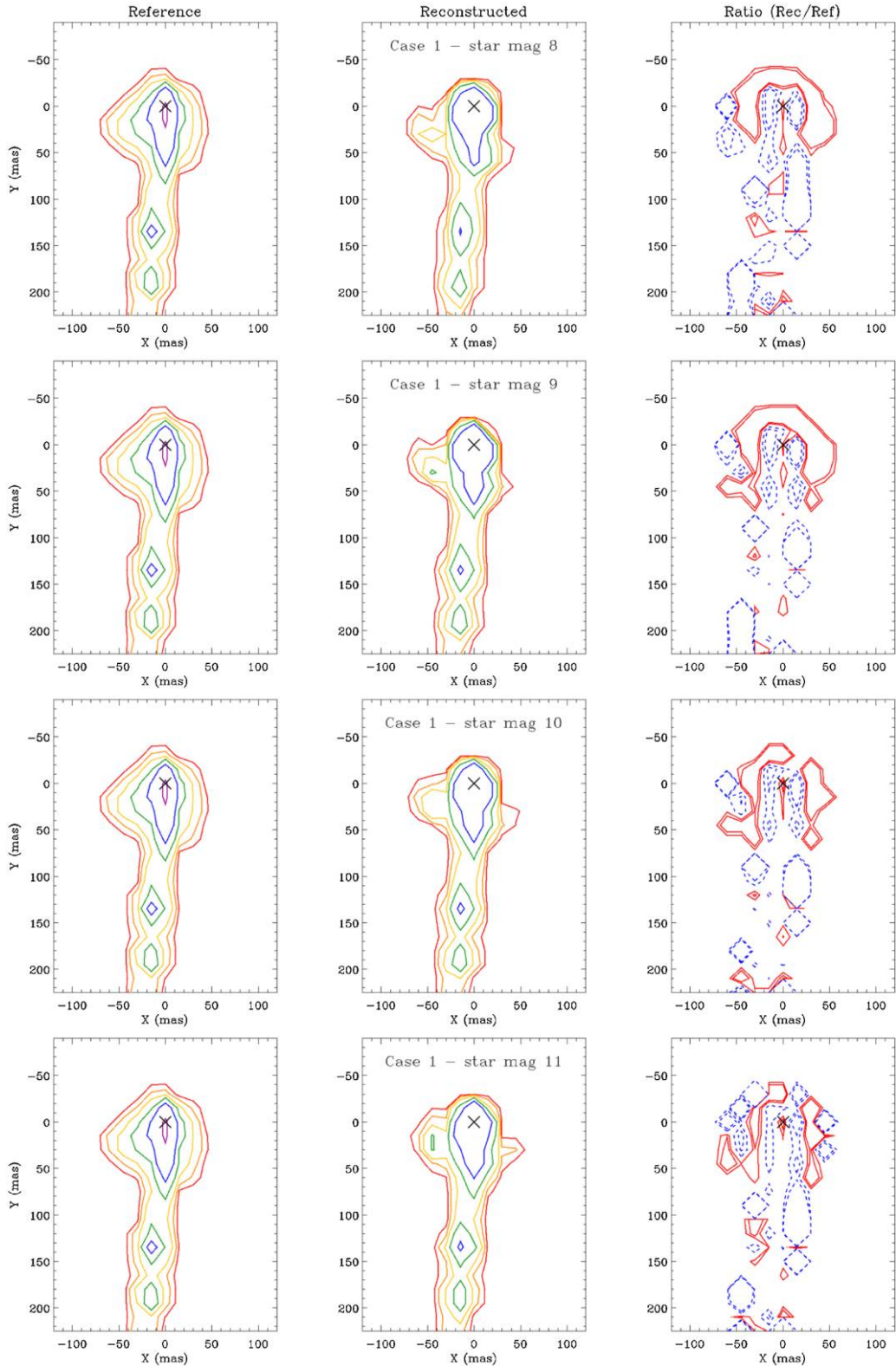


FIG. 6.—Contour plots for reference object (*left*), reconstructed object (*center*), and ratio object (reconstructed/reference) (*right*) for Case 1 (single dish observations). The four rows refer to the different central star magnitudes we have analyzed. Contour levels of the ratio image are: 0.67, 0.83 (*both in solid red lines*), and 1.2, 1.5 (*in dashed blue lines*). These contours mark areas where the flux of the reconstructed image is lower (*red*) or higher (*blue*) by a factor 1.2 and 1.5 with respect to the reference image. Distances (in mas) are computed from the position of the star (*black cross*). See the electronic edition of the *PASP* for a color version of this figure.

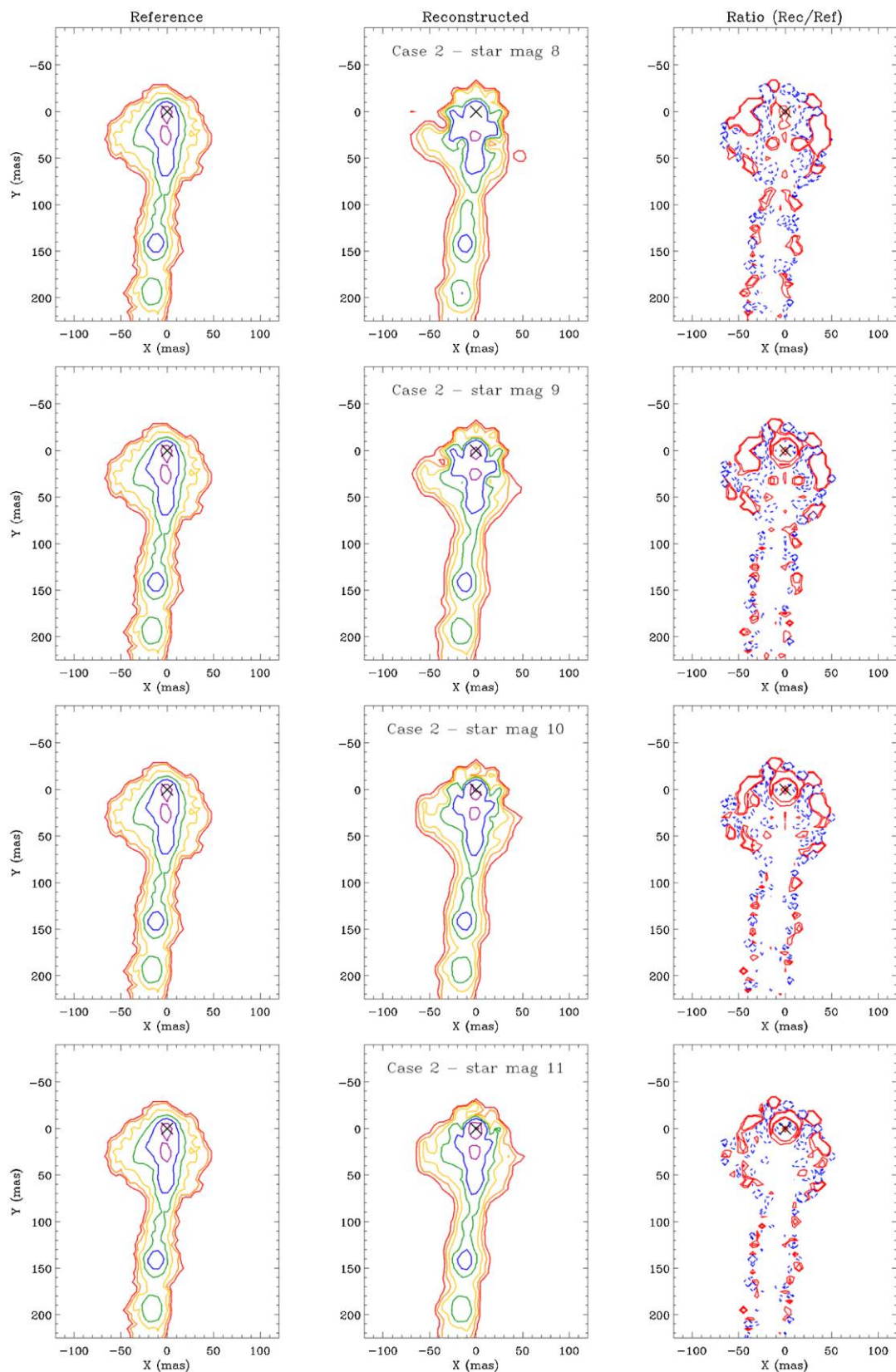


FIG. 7.—Same as Fig. 6 for Case 2 (interferometric observations). See the electronic edition of the *PASP* for a color version of this figure.

orthogonal to its axis, and the jet morphology (in particular width and position of emission knots). The total profile flux is displayed in Figures 4 and 5 as a function of the distance from the central star for Cases 1 and 2, respectively, one separating the region around the star (~ 200 mas) and the other including the remainder of the jet. The integrated profile fluxes relative to the four scenarios with different central star magnitude are plotted with different linestyles and colors. Finally, a relative error with respect to the original image is also plotted for a direct evaluation of the goodness of the reconstruction.

In both cases, the MC-RL method provides a very good photometric reconstruction of the jet region at a distance > 200 mas, with relative errors always below 20%. This region is not affected by the effects of the image of the central star; therefore there is basically no difference in the four cases with varying star magnitudes. The inspection of the inner region shows that the total intensity is very well reconstructed down to the central source (relative error less than 20% in both Case 1 and 2) for central star magnitudes fainter than 9 mag. The error increases, up to 30%–40% at worst, in the case of the 8 mag star.

To evaluate the overall morphology in the region close to the star we display in Figures 6 and 7 the contour plots of the original image, the reconstructed one, and their ratio (reconstructed/

original) in the jet innermost region (covering about 200 mas), again for all the considered cases. These contour plots put into evidence where the reconstruction produces the largest discrepancies in morphology with respect to the original jet, thus hampering the analysis of the jet structure. The inspection of the two figures shows that a very good reconstruction, deviating by no more than 20% from the original image, is obtained in the jet core for distances $\gtrsim 50$ mas for Case 1 and $\gtrsim 20$ mas for Case 2, independent of the central star magnitude. Larger deviations occur, as expected, at the edge of the jet profile, where the flux decreases.

The effects of these edge deviations can be visualized in Figures 8 and 9, respectively, where we plot the measured width (at half maximum) of the jet profile in the original and reconstructed images as a function of the distance from the source. From these figures, we can evaluate the limits that we encounter in the correct derivation of the jet width as a function of the distance (d). We can see that in Case 1 the width of the jet is well reproduced at $d > 60$ mas for a central star magnitude ≥ 9 mag and at $d > 75$ mas for the case of a central star of 8 mag. Regarding the LN images, a good measure of the width is obtained down to 20 mas, for star magnitudes > 10 mag, which degrades to about 30 mas for the brighter star cases.

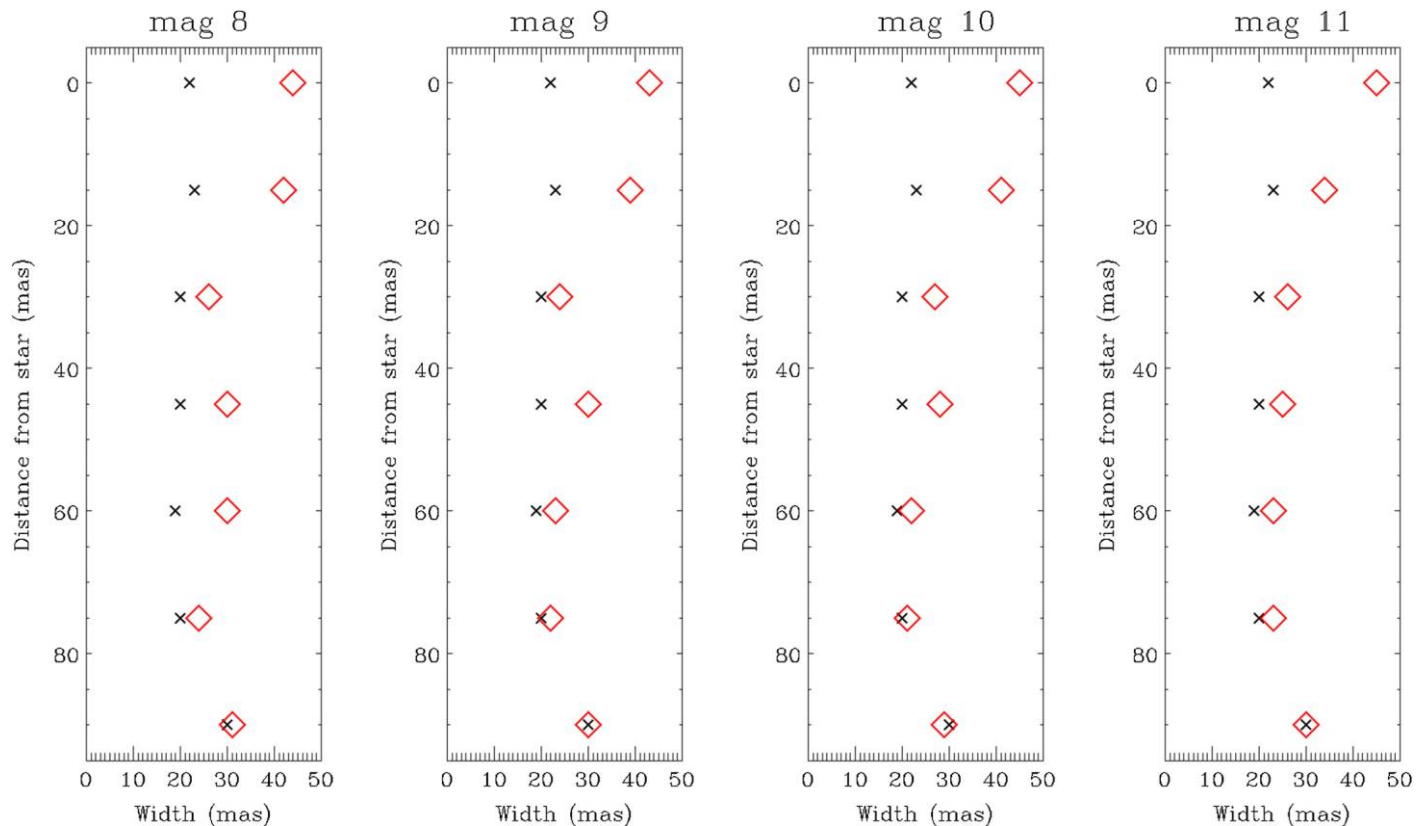


FIG. 8.—Case 1 observations: measured width (at half maximum) of the spatial profile of the jet (in the direction orthogonal to its axis) for the reference image (black cross) and reconstructed image (red diamond) for increasing distances from the star. The four panels refer to the different central star magnitude cases. See the electronic edition of the *PASP* for a color version of this figure.

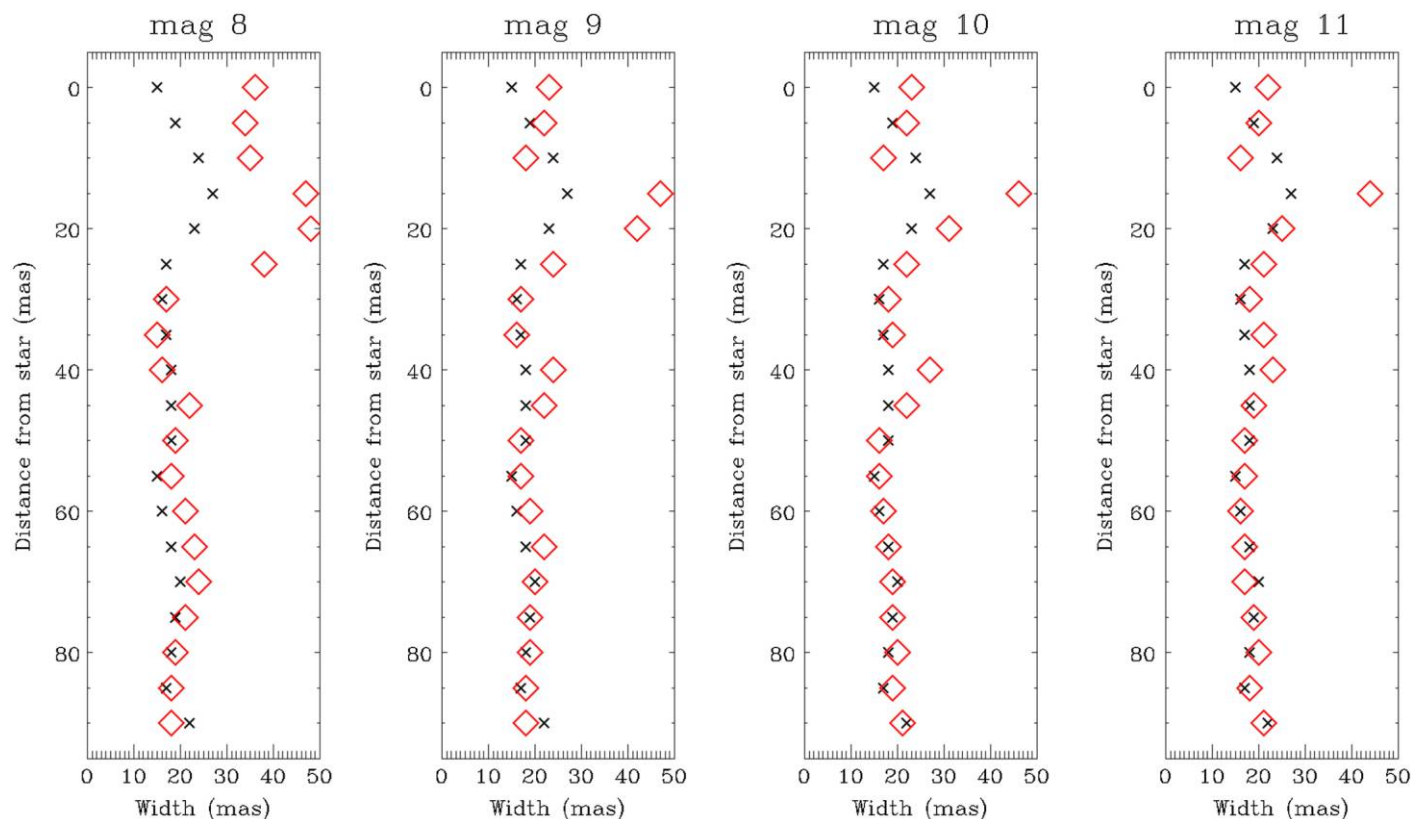


FIG. 9.—Same as Fig. 8 for Case 2 (interferometric observations). See the electronic edition of the *PASP* for a color version of this figure.

We point out that this kind of measurement represents the actual scientific analysis we plan to perform on the real jet images, because the derivation of the jet width as near as possible to the driving source provides precious information on the jet collimation degree, and eventually on its launching mechanism. For reference's sake, we note that a distance of 50 mas corresponds to about 8 AU for a jet placed at 150 pc, i.e., well within the region of acceleration of the jet according to the current models (e.g., Frank et al. 2013). The simulation thus suggests that the presented reconstruction method allows us to effectively investigate the innermost region of the jet, providing important constraints, even if applied to single dish images taken on 10 m-class telescopes.

5. CONCLUSIONS

We considered simulated observations of a YSO jet with a single dish 10 m class telescope (Case 1) and with the LBT/LINC-NIRVANA interferometric instrument (Case 2), and then analyzed the image reconstruction process. Observations of jets from young stars provide a typical example of high dynamic range data (the faint extended jet line emission is detected together with the strong signal from the star) for which common deconvolution methods like Richardson-Lucy do not produce good results. In this framework, we proposed and

discussed a new method for image reconstructions, named *multi-component Richardson-Lucy* (MC-RL), in which the image we want to retrieve is treated as the sum of two components (star and jet). After introducing a regularization parameter for the second term, the reconstructed image is eventually obtained through iterations alternating between the two components.

The conclusions of our work can be summarized as follows:

1. Our MC-RL method provides more accurate results than the standard Richardson-Lucy method as it is able to effectively reduce the number of artifacts in the region close to the star. However, it can be improved in several directions. First, the regularization term can be replaced by the ℓ_2 norm of the modulus of the gradient or of the Laplacian of the object in order to enforce smoothness of the solution. Both regularizers can be easily treated by means of the SGM method proposed by Lantéri et al. (2002). Secondly, the efficiency of the algorithm, which is quite slow, can be considerably improved by replacing the scaled gradient method, used in this paper, with the scaled gradient projection (SGP) method proposed by Bonettini et al. (2009) (see also Prato et al. 2012). Finally, the crucial problem of the choice of the regularization parameter can be solved by means of the recently proposed method of the so-called *Bregman iterations* (Benfenati & Ruggiero 2013).

2. For our simulations we have considered four different jet-star contrasts (jet integrated magnitude of 14.5 mag versus star magnitude varying from 8 to 11 mag). From the analysis of the reconstructed objects, we derive that the MC-RL method allows us to, in Case 1, evaluate down to 60 mas (75 mas) both the width and the intensity of the jet with an accuracy better than about 20%, if the central star magnitude is fainter (brighter) than about 9 mag; and in Case 2 to estimate down to 20 mas (30 mas) the width of the jet if the central star is fainter (brighter) than 10–11 mag, and to derive the integrated profile flux with an accuracy better than about 20% in all the considered cases. These limits allow us to obtain a satisfactory sampling of the jet acceleration region, which is expected to occur within about

50 AU (i.e. 0.3 arcsec at a distance of 150 pc) from the jet driving star.

3. As a future development of our work, we plan to analyze the images reconstructed through the MC-RL method in the broader case of simulated observations with upcoming extremely large telescopes.

This work has been partially supported by INAF (Istituto Nazionale di AstroFisica) under the contract TECNO-INAF 2010 “Exploiting the adaptive power: a dedicated free software to optimize and maximize the scientific output of images from present and future AO facilities.”

REFERENCES

- Agra-Amboage, V., Dougados, C., Cabrit, S., & Reunanen, J. 2011, *A&A*, 532, A 59
- Anconelli, B., Bertero, M., Boccacci, P., Carbillet, M., & Lantéri, H. 2006, *A&A*, 448, 1217
- Arcidiacono, C., Diolaiti, E., Tordi, M., et al. 2004, *Appl. Optics*, 43, 4288
- Ayasso, H., Rodet, T., & Abergel, A. 2012, *Inverse Problems*, 28, 125005
- Bardsley, J. M., & Goldes, J. 2009, *Inverse Problems*, 25, 095005
- Barrett, H. H., & Meyers, K. J. 2003, *Foundations of Image Science* (Hoboken: Wiley)
- Benfenati, A., & Ruggiero, V. 2013, *Inverse Problems*, 29, 065016
- Bertero, M., & Boccacci, P. 2000, *A&AS*, 147, 323
- . 2005, *A&A*, 437, 369
- Bertero, M., Boccacci, P., Desiderà, G., & Vicidomini, G. 2009, *Inverse Problems*, 25, 123006
- Bertero, M., Boccacci, P., La Camera, A., Olivieri, C., & Carbillet, M. 2011, *Inverse Problems*, 27, 113001
- Bertero, M., Boccacci, P., Talenti, G., Zanella, R., & Zanni, L. 2010, *Inverse Problems*, 26, 10500
- Bonettini, S., Zanella, R., & Zanni, L. 2009, *Inverse Problems*, 25, 015002
- Carbillet, M., Vérinaud, C., Femenía, B., Riccardi, A., & Fini, L. 2004, *MNRAS*, 356, 1263
- Ciliegi, P., La Camera, A., Desiderà, G., et al. 2008, *Proc. SPIE*, 7013, 701335
- Csiszár, I. 1991, *Ann. Stat.*, 19, 2032
- De Mol, C., & Defrise, M. 2004, in *Proc. Int. Symp. on Electromagnetic Theory* (Pisa, Italy), 798–800
- Desiderà, G., & Carbillet, M. 2009, *A&A*, 507, 1759
- Desiderà, G., La Camera, A., Boccacci, P., Bertero, M., & Carbillet, M. 2008, *Proc. SPIE*, 7013, 701340
- Donoho, D. L., Johnstone, I. M., Hoch, J. C., & Stern, A. S. 1992, *J. R. Stat. Soc. B*, 54, 41
- Frank, A., Ray, T., Cabrit, S., et al. 2013, *Protostar & Planets VI* (Tucson: University of Arizona), in press
- Giovannelli, J.-F., & Coulais, A. 2005, *A&A*, 439, 401
- Herbst, T., Ragazzoni, R., Andersen, D., et al. 2003, *Proc. SPIE*, 4838, 456–465
- Hill, J. M. 2010, *Appl. Opt.*, 49, D 115
- Hook, R. N., & Lucy, L. B. 1994, in *The Restoration of HST Images and Spectra II (STScI)*, ed. R. J. Hanish, & R. L. White, 86–94
- Konigl, A., & Pudritz, R. E. 2000, *Protostars and Planets IV* (Tucson: University of Arizona), 759
- La Camera, A., Antonucci, S., Bertero, M., et al. 2012, *Proc. SPIE*, 8445, 84453D
- Lantéri, H., Roche, M., & Aime, C. 2002, *Inverse Problems*, 18, 1397
- Lucy, L. B. 1974, *AJ*, 79, 745
- Lucy, L. B. 1994, in *The Restoration of HST Images and Spectra II (STScI)*, ed. R. J. Hanish, & R. L. White, 79–85
- Nisini, B., Caratti o Garatti, A., Giannini, T., & Lorenzetti, D. 2002, *A&A*, 393, 1035
- Prato, M., Cavicchioli, R., Zanni, L., Boccacci, P., & Bertero, M. 2012, *A&A*, 539, A 133
- Reipurth, B., Heathcote, S., Morse, J., Hartigan, P., & Bally, J. 2002, *AJ*, 123, 362
- Richardson, W. H. 1972, *J. Opt. Soc. America*, 62, 55
- Snyder, D. L., Hammoud, A. M., & White, R. L. 1994, *J. Opt. Soc. Am.*, A 10, 1014
- Snyder, D. L., Helstrom, C. W., Lanterman, A. D., Faisal, M., & White, R. L. 1995, *J. Opt. Soc. Am.*, A 12, 272